Available online at www.sciencedirect.com

ScienceDirect

journal homepage: www.elsevier.com/locate/he

Graphitic carbon nitride (g-C_3N_4) decorated with Yttrium as potential hydrogen storage material: Acumen from quantum simulations

Pratap Mane [a,*], *Antara Vaidyanathan* [b], *Brahmananda Chakraborty* [c,d,**]

[a] *Seismology Division, Bhabha Atomic Research Centre, Trombay, Mumbai 400085, India*
[b] *Department of Chemistry, Ramnarain Ruia Autonomous College, Mumbai, 400019, India*
[c] *High Pressure and Synchrotron Radiation Physics Division, Bhabha Atomic Research Centre, Trombay, Mumbai 400085, India*
[d] *Homi Bhabha National Institute, Mumbai 400085, India*

HIGHLIGHTS

- Y atom bind strongly at hollow porous space of g-C_3N_4 with binding energy −6.85 eV.
- Maximum of 9H_2 molecules adsorbed on gCN + Y system with wt % of hydrogen as 8.55.
- Average desorption temperature of 384.24K, optimum for fuel cell application.
- Y doped g-C_3N_4 stable at higher temperatures upto 500K verified by MD simulations.
- Charge donation from Y to H_2 is due to the Kubas interactions.

GRAPHICAL ABSTRACT

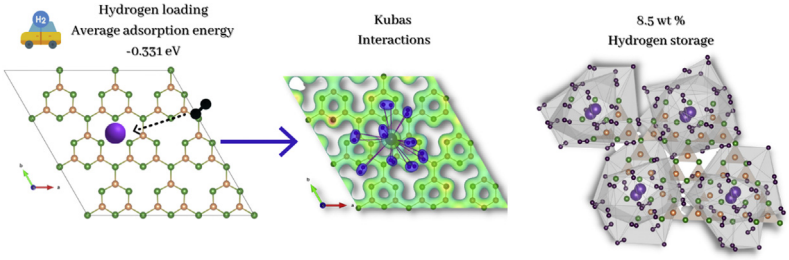

ARTICLE INFO

Article history:
Received 2 December 2021
Received in revised form
17 April 2022
Accepted 19 April 2022
Available online 12 May 2022

Keywords:
Reversible hydrogen adsorption
Density functional theory

ABSTRACT

With the aid of the state-of-the-art Density Functional Theory simulations, triazine-like graphitic carbon nitride or g-C_3N_4 (abbreviated as gCN hereafter) nanosheet decorated with Y has been explored for reversible hydrogen storage applications in light fuel cell vehicles. The Y atom is found to bind strongly with gCN (binding energy ~ −6.85 eV), can reversibly store 9 H_2 with an average adsorption energy of −0.331 eV/H_2, an average desorption temperature of 384.24 K, and a storage capacity of 8.55% by weight, optimum for fuel cell application as prescribed by the Department of Energy. The bonding of Y on gCN involves a charge transfer from Y 4d orbitals to C and N 2p orbitals, whereas the adsorption of H_2 is due to Kubas interactions involving net charge transfer from Y 4d orbital to H 1s orbital. We have computed the diffusion energy barrier for Y atoms as 3.07 eV, which may

* *Corresponding author.*
** *Corresponding author.* High Pressure and Synchrotron Radiation Physics Division, Bhabha Atomic Research Centre, Trombay, Mumbai 400085, India.
E-mail addresses: pratapm@barc.gov.in (P. Mane), brahma@barc.gov.in (B. Chakraborty).
https://doi.org/10.1016/j.ijhydene.2022.04.184

Molecular dynamics
Fuel cell application

prevent metal-metal clustering. Further, ab-initio molecular dynamics simulation has been performed to check the structural stability of the present system. The system is found to be stable at 500 K with different concentrations of Y doping. The present system with the appropriate average adsorption energy per H_2, suitable desorption temperature, and structural stability at higher temperatures is promising for onboard light fuel cell applications.

Introduction

The global energy and climate crises have prompted a search for alternative fuels that do not emit carbon dioxide or carbon monoxide [1]. Hydrogen, being highly energy-intensive and abundantly available by photo- or electro-lysis of water is considered to be a highly potent fossil fuel alternative [2–7]. With an energy density higher than known hydrocarbon-based fuels, and the possibility of combustion to produce only water as a by-product, hydrogen as a fuel is appealing to the current societal needs [8,9]. Further, it can be integrated into fuel cells, allowing for its use as a transport fuel in Fuel Cell Vehicles (FCVs). However, for light vehicles, the ideal transport fuel must have certain characteristics to be accommodated onboard. Hydrogen in its compressed gaseous or liquid form can be stored in cylinders under pressure; however, these are bulky and inconvenient for light vehicles. A popular technique for liquid storage [10] is Liquid Organic Hydrogen Carriers (LOHCs) in which hydrogen lean molecules act as adsorbents via chemisroption for hydrogen storage, accompanied by hydrogen release through catalytic dehydrogenation [11]. Although, these systems are attractive, their low hydrogen storage capacity can limit their applicability [12]. Recently, Tarhan et al. [13] has compared the various onboard hydrogen storage methods and concluded that solid state storage is more promising than other techniques. Thus, a better solution for onboard hydrogen storage and transport for light vehicles is its reversible adsorption on a solid substrate. Hydrogen adsorption in a reversible manner requires the substrate material to load hydrogen at low temperatures and high pressures, and unload upon requirement through triggers such as elevated temperatures and low pressures. In this respect, the United States Department of Energy (DoE) [14] has prescribed requirements for substrate materials that can be used for onboard hydrogen storage applications, wherein an average adsorption energy between 0.2 and 0.7 eV per H_2, desorption temperatures of ~400 K, and storage capacity > 6.5% by weight, are included.

Metal hydrides have been extensively studied for hydrogen storage applications. In the case of metal hydrides, hydrogen forms a chemical bond with metal or metal alloys. Magnesium hydride shows a high energy density as compared to other metal hydrides with a reversible hydrogen storage capacity of 7.7% [15–17]. Chemisorbed hydrogen may give excellent gravimetric hydrogen storage capacities well above the DOE's requirements; however high desorption temperatures and sluggish adsorption-desorption kinetics are the major deterrents [18,19]. Intermetallic systems like alloys are also being explored to overcome the shortcomings of metal hydrides. These intermetallic alloys ($A_mB_nH_x$ where A and B are metals) have shown promise towards onboard hydrogen storage applications, particularly of the types AB_2, AB_5, and A_2B [20]. Hydrogen storage capacities of some common intermetallic hydrides like $LaNi_5H_6$, $FeTiH_2$, Mg_2NiH_4, and $ZrMn_2H_2$ are 1.37, 1.89, 3.59, and 1.77% respectively, falling short of the required capacity set by DoE [21].

Carbon nanomaterials like activated carbon, graphite, graphene, graphyne, MWCNT, fullerenes, MXene etc., have also been explored in this respect [7,22–29]. Activated carbon is a high-performance material with a large specific surface area of 3000 m^2/g and nanoscale pores of about 1 nm or lesser, consisting of nanocrystallites of graphite and amorphous carbon. Storage capacities for hydrogen of up to 5.7% have been attained [30]. Various studies also directed towards enhancing adsorption properties by metal doping and chemical treatments, with KOH treated, Ni-doped, Pd-doped, and Pd-doped activated carbon providing hydrogen storage capacities of 6.6, 1.8, 2.3, and 5.5% respectively [23–25,31]. The most optimum performance of activated carbon requires lower temperatures of ~77 K which may be unfavorable for onboard hydrogen storage applications [32].

Metal doped/decorated carbon nanotubes have been investigated for hydrogen storage applications. Multiwalled carbon nanotubes (MWCNT) with Pd nanoparticle decoration were reported to show 6 wt% hydrogen storage capacity. Theoretical investigations of Ti- and Y- doped SWCNT revealed 5.7 [33] and 6.1% [34] capacity respectively, with binding energies of 0.18 eV and 0.41 eV per H_2. The advent of graphene paved the way for developing two-dimensional (2D) materials for hydrogen storage applications. Two-dimensional materials are especially suited for the purpose due to their high specific surface area, and often enhanced electronic properties that allow for stronger hydrogen binding that makes the loading and unloading of hydrogen on these materials apt [35,36]. Graphene presents excellent opportunities in electron-exchange type interactions with hydrogen for storage applications owing to the surface moieties at its sheet edges, rendering the material with unusual electronic properties. As compared to pristine graphene, however, the presence of metal doping or impurities can allow for the spillover effect enhancing hydrogen storage capacities [37].

Recently, modified pentagraphene has been explored for its hydrogen storage potential with Li-doped pentagraphene decorated with Li giving an output of 7.88% hydrogen storage,

with adsorption energy of hydrogen falling in the range of 0.1–0.4 eV [37]. Another Li-decorated graphene-based hydrogen storage substrate was developed computationally using porous graphene frameworks using three different organic linkers with 4,40,400-(benzene-1,3,5triyl-tris (benzene-4,1-diyl))tribenzoate (BBC))-based graphene structure with 160 Li atoms. It showed an excellent hydrogen uptake capacity of 4.26% at ambient temperatures and 100 bars pressure [28]. Few-layered graphene (FLG) prepared by a novel plasma-induced exfoliation showed a hydrogen storage capacity of about 2 wt% at 77 K [38]. Vinayan et al. prepared N-doped graphene by in situ synthesis, and carried out Pd decoration through a green synthesis method. The resulting heterostructure gave 4.5 wt% hydrogen storage capacity at room temperature and 4 MPa pressure [39]. By incompletely etched MXene using hydrofluoric acid, a multilayered Ti_2CT_x has been proposed as a superior hydrogen storage material with hydrogen uptake of 8.8 wt% at room temperature and 60 bar H_2 [22], which retains ~4 wt% hydrogen even at ambient conditions (25 °C, 1 bar air).

Density-functional-theory-(DFT)-based studies have also been conducted on graphene sheets. Ti-decorated sheets of porous graphene demonstrate hydrogen storage ability of 6.11 wt% through theoretical studies [40]. Another DFT study involving Ti-doping investigated the hydrogen storage capabilities of the recently proposed ψ-graphene, which gave excellent storage capacities of 13.14 wt% and a binding energy of −0.3 eV per H_2 [41]. Ti- and Zr-doped graphene gave 7.8 and 11 wt% hydrogen storage capability respectively with binding energies of 0.42 eV and 0.34 eV per hydrogen molecule. Another novel material, Zeolite templated carbon (ZTC) has shown promise in hydrogen storage applications, with Li-functionalized ZTC giving a gravimetric storage capacity of 6.78% [42], while another work by the same group involved a ZTC vacancy substituted by boron as a potent hydrogen storage substrate giving a storage capacity of 6.55 wt% and binding energy of ~0.2 eV per H_2 [43].

Heterostructures of carbon and nitrogen such as triazine frameworks have been reported as potential hydrogen storage substrates [44]. Zr-decorated covalent triazine frameworks (CTF-1) have shown promise in a DFT-based study, with a binding energy of ~0.4 eV, storage capacity of 7.1%, and a desorption temperature of 442 K [45]. Li-doped g-C_2N has been reported as a potential hydrogen storage substrate giving a maximum gravimetric hydrogen uptake of 7.8% [46]. Another work involved Mg decoration over g-CN that had a heptazine structure, was found to give favorable hydrogen storage of 7.8% with binding energies ranging from ~0.13 to 0.28 eV [47]. The presence of heteroatoms like N in a carbon-based framework can invoke the heteroatom effect, thereby modifying the electronic properties of such materials, which could translate to an improved performance in applications involving charge-based interactions [48].

Graphitic carbon nitride is another potent and promising material for energy storage applications [49]. Triazine-based graphitic carbon nitride (gCN) is a polymeric semiconductor consisting of alternating C–N bonds forming hexagonal triazine rings linked to one another through bridging N atoms forming a highly porous substrate. The entire 2D structure being sp^2 hybridized lends aromaticity to the structure, as well as high electron mobility due to the π-electron cloud formed above and below the plane [50]. Further, gCN offers a tunable and narrow bandgap opening up avenues for various electronic applications. Moreover, gCN can be synthesized by facile methods and has high stability. Tan et al. (2015) proposed a switch mechanism for loading and unloading hydrogen with hydrogen adsorption capacity of 6–7 wt% by First Principles calculations [51]. Nair et al. (2015) achieved a room temperature storage capacity of 3.4 wt% at pressures of up to 4 MPa in Pd nanoparticle decorated gCN [52]. If decorated or doped with early transition metals, Kubas bonding [53] can be invoked, wherein a charge transfer from the bonding molecular orbitals of hydrogen towards the vacant TM d orbitals occurs, follwed by a back donation of charge from the TM d orbitals towards the vacant antibonding molecular orbitals of hydrogen [54].

In this work, by First Principles investigations, we have decorated gCN with Y atom to enhance the electronic properties and adsorption capacity towards hydrogen for reversible, onboard storage applications in light FCVs. We have analyzed the optimum locations for the Y atom to relax over the gCN structure using their corresponding adsorption energies and investigated the binding mechanism of Y over gCN through charge transfer analysis and density of states (DOS) analysis. We have arrived at the maximum hydrogen storage capacity by consulting the average adsorption energies of hydrogen on methodical loading of hydrogen molecules on Y-decorated gCN (Y-gCN). The binding mechanism of hydrogen over Y-gCN has also been investigated. Further, we have addressed the possibility of Y clustering over gCN by computing the diffusion energy barrier for its movement across the gCN plane. Practical feasibilities of the system, such as stability at the highest desorption temperature have been examined by ab-initio Molecular Dynamics (MD) simulations conducted at 500 K.

Computational details

All DFT calculations in this work were conducted by the Vienna ab initio Simulation Package (VASP) code [55–57], making use of the Projector Augmented Wave (PAW) method. We used a 3 × 3 supercell of triazine based g-C_3N_4 (gCN) having cell dimensions of 14.37 Å × 14.37 Å with the interference of periodic layers avoided by inserting an interlayer vacuum of 20 Å. The convergence study for vacuum inserted in z-direction is provided in supplementary data Table S1. The basis set restriction was accomplished by a plane wave-cut off set to 500 eV, and a 7 × 7 × 1 K-point mesh of the Monkhorst-Pack special scheme was used to sample the Brillouin Zone. The detailed convergence study of the cut-off energy and Kpoints is given in Supplementary Table S2. Geometric optimization was conducted by conjugate gradient methods with a convergence criterion of 0.01 eV/Å for interatomic forces and 10^{-5} eV for total energy. The accuracy of DFT simulations is highly sensitive to the choice of the exchange correlation functional used. The Local Density Approximation (LDA) tends to overestimate binding interactions because it approximates the electron density to a homogenous electron cloud [58]. The Generalized Gradient Approximation (GGA)

underestimates binding energy as it considers a gradient of electron density. Long-range interaction forces like van der Waals (vdW) become highly relevant in weak-field interactions which may occur in hydrogen adsorption over substrate materials. To improve on the exchange-correlation functional as best as possible, we have used the GGA functional as described by Perdew et al. (PBE-GGA) [59,60], and accounted for long-range forces employing additional dispersion corrections as prescribed by Grimme's DFT-D2 scheme [61]. For a more accurate computation of the bandgap, we have used the hybrid functional described by Heyd–Scuseria–Ernzerhof (HSE06) which contains a part of the exact Hartree-Fock exchange energy [62].

Results and discussion

Structure and properties of gCN

A 3 × 3 supercell of gCN made of 27 atoms of C and 36 atoms of N (for more details on the atomic positions of the supercell, refer to the supplementary data) was geometrically optimized, the structural plot of which is represented in Fig. 1 (a and b). The structure is found to be planar, with π conjugation over the plane as each C and N atom in the structure is sp^2 hybridized, with lattice parameters of 14.37 Å × 14.37 Å upon relaxation. The average C–N bond length is found to vary within the ring and bridging C–N–C bonds as 1.33 Å and 1.47 Å respectively, corroborating reasonably well with the previously reported value of 1.32 Å and 1.44 Å in theoretical work [63]. To investigate the electronic and magnetic properties of the system, a total density of states (TDOS) analysis was carried out as displayed in Fig. 1(c). From the TDOS plot, it is apparent that the material is non-magnetic owing to the spin symmetry in the UP and DOWN spin channels, and has a bandgap of 1.6 eV by the GGA-PBE functional, which is lower than the experimentally reported value of 2.72 eV. The difference in the bandgap of theoretical work and experimental work can be attributed to drawbacks in the exchange-correlation functional which vastly underestimates band gaps [45]. Exchange correlation functionals with a part of the Hartree-Fock estimations as implemented in hybrid functionals give more accurate estimations of the bandgap. In this case, we have computed the bandgap by DOS analysis using the Heyd-Scuseria-Ernzerhof (HSE06) [64] hybrid functional as 2.868 eV, which matches well with the experimentally reported value of 2.72 eV [65].

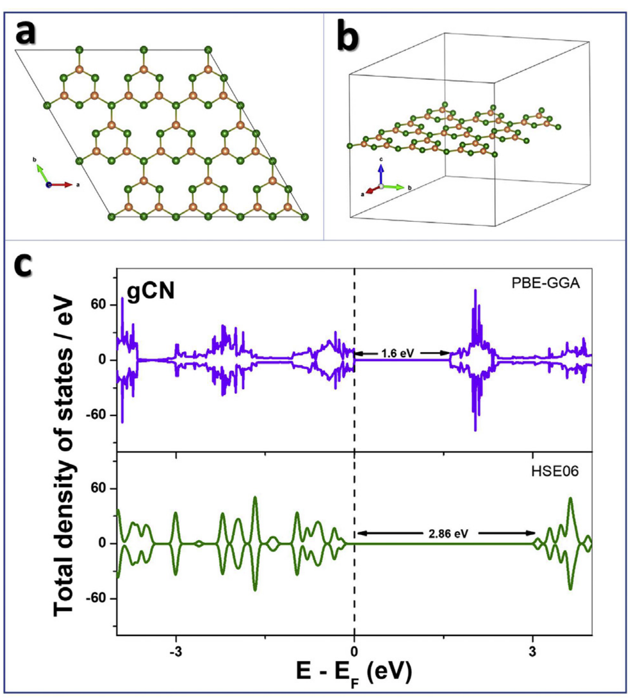

Fig. 1 – Relaxed structure of gCN in top view (a), side view (b), and TDOS of relaxed gCN with C and N atoms represented by orange and green spheres respectively by GGA-PBE exchange-correlation functional in the top panel and HSE06 hybrid functional in the bottom panel (c). Fermi level is set to zero eV. (For interpretation of the references to color in this figure legend, the reader is referred to the Web version of this article.)

Decoration of Y on gCN

The relaxed structure of gCN was then used for investigating the interactions between Y and gCN. A single Y atom was placed at a distance of 2 Å above the plane of gCN, and the resulting structure was allowed to relax. To identify the most likely locations of decoration of Y atom on the gCN surface, we selected four possible locations, A- hollow above triazine rings, B- bridge site of C–N bonds, C- bridge site of triazine C–N bonds, and D- hollow between three triazine rings. The doping locations are depicted in Fig. 2(a). All four resulting structures were relaxed and the binding energy of the Y atom over gCN was calculated for all cases using the following mathematical expression:

$$E_b = E_{gCN+Y} - E_{gCN} - E_Y \quad (1)$$

where E_{gCN+Y}, E_{gCN}, and E_Y are respectively, the energy of Y-decorated gCN, the energy of gCN, and the energy of an isolated Y atom. The stability of the structure can be judged from the more negative binding energy as a result of the lowering of E_{gCN+Y} as compared to its counterparts. The most negative binding energy signaling the optimum decorating location is found to be at the top site between three triazine rings or location D, with a binding energy of −6.852 eV. The relaxed structure of gCN + Y in this location (hereby mentioned as gCN + Y) is represented in Fig. 2(b).

In the relaxed structure of gCN + Y, the Y atom is found to align at the top site of the hollow such that the average distance between Y and N atoms of neighboring triazine rings is 2.294 Å. The introduction of Y is also accompanied by a slight distortion of planarity, evident from the relaxed gCN + Y side view in Fig. 2(b). The average C–N bond lengths in the neighboring triazine rings distend to 1.36 Å while the bridging C–N bonds remain more or less at the same length. Besides structural changes, the changes in electronic and magnetic properties of gCN on decorating with Y are explored in the TDOS analysis represented in Fig. 3. Y-decoration brings with

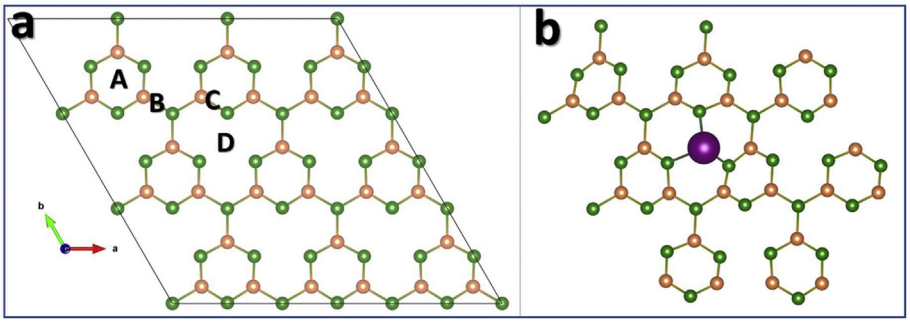

Fig. 2 – Various locations for placing Y atom over the relaxed structure of gCN (a), Relaxed structure of gCN + Y in most favorable binding location, with Y atoms represented by purple sphere (b). (For interpretation of the references to color in this figure legend, the reader is referred to the Web version of this article.)

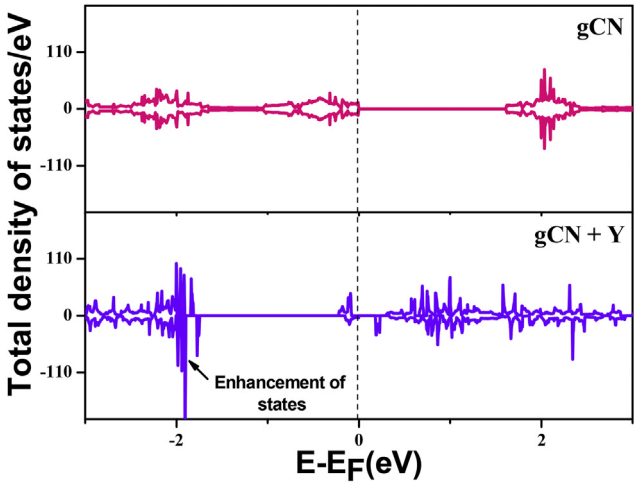

Fig. 3 – TDOS of gCN (top panel) compared with that of gCN + Y (lower panel). Fermi level is set to zero eV.

it a reduction in band gap to 0.17 eV, a loss of symmetry in UP and DOWN spin channels resulting in a net magnetic moment of $1\mu_B$, as well as some enhancement of states at the Fermi level and around −2 eV in the valence band.

Adsorption of hydrogen over Y-gCN

Now, to the relaxed gCN + Y an H_2 molecule is introduced at a distance of 2 Å followed by systemic relaxation. The relaxed structure of gCN + Y+ $1H_2$ is depicted in Fig. 4(a). The H_2 molecule adsorbs over gCN + Y with an average Y–H distance of 2.455 Å, whereas the average Y–N bond distances distend to 2.361 Å. The bond length between H–H in a free hydrogen molecule is 0.75 Å, whereas upon adsorption over Y-gCN, the bond elongates slightly to 0.77 Å; however, the elongation occurs without dissociation of H_2. The adsorption energy of hydrogen molecule over gCN + Y was calculated utilizing the following expression:

$$E_{ad} = \left(E_{gCN+Y+nH_2} - E_{gCN+Y} - nE_{H_2}\right)/n \quad (2)$$

where E_{ad}, $E_{gCN+Y+nH_2}$, and nE_{H_2} represent average adsorption energy (eV/H_2) of hydrogen over gCN + Y, the energy of gCN + Y + nH_2, and the energy of free nH_2 molecules respectively. The average adsorption energy of the first adsorbed hydrogen was computed to be −0.672 eV while for the 9th H_2 molecule it is −0.331 eV. The adsorption energy for the first H_2 molecule is higher than that for the others. There is a decrease of adsorption energy to −0.2 to −0.4 eV for the farther nH_2 (n = 4–9) molecules. This is indicative of an easy desorption for most of the H_2 molecules within the desirable adsorption energy range [66]. We then introduced H_2 step-wise over gCN + Y with systemic relaxation carried out at each stage. It was found that gCN loaded with Y atom (surface + metal) can adsorb a maximum of 9 H_2 reversibly. The relaxed structures for gCN + Y+ $3H_2$ to gCN + Y+ $9H_2$ are depicted in Fig. 4(b–e) respectively. The first H_2 is adsorbed at an average distance of 2.45 Å from the Y atom. The farthest H_2 molecules adsorb at an average distance of 4.1–4.3 Å from the Y atom. The corresponding average H–H bond distances for the adsorbed hydrogen molecules elongate to 0.78 Å from the initial value of 0.75 Å indicating charge transfer and adsorption by all H_2 molecules. For more details about the H–H and Y–H bond distances for nH_2 (n = 1–9), refer to Supplementary Table S3. The vertical distance between Y and the plane of the gCN sheet with no H_2 and with maximum H_2 elongates from 2.30 Å to 2.34 Å, respectively. The slight increase in the vertical distance (0.04 Å) is in agreement with a previously reported double carbon graphene doped Y hydrogen adsorption system [66]. Since the position of Y changes after H_2 adsorption, hydrogens are absorbed not only by the Y atom but the overall adsorption is on the surface + metal system. To compute the maximum H_2 uptake, we have considered the average adsorption energy as an essential criterion for fulfilling the DOE's requirements. Further, the other criteria as earlier suggested by Fair et al. [66] such as i) the distance between 1st and last H_2 from the dopant, ii) vertical distance between the metal atom and the plane of the gCN sheet with no H_2, the same quantity but with maximum H_2, iii) the ranges of H–H bond distances, iv) the charge transfer analysis (refer charge density plots provided below), and v) the estimated maximum H_2 storage capacity from ab initio MD study (Supplementary Fig. S1) have been considered to verify the overall uptake of 9 H_2 molecules by the gCN + Y system.

From an inspection of the optimized atomic structures (taking into account dopant to nH_2 distance) and the corresponding change in the adsorption energy, the maximum uptake of H_2 can be considered. The H–H bond elongations, charge density plots, and MD simulations with maximum H_2 uptake further support

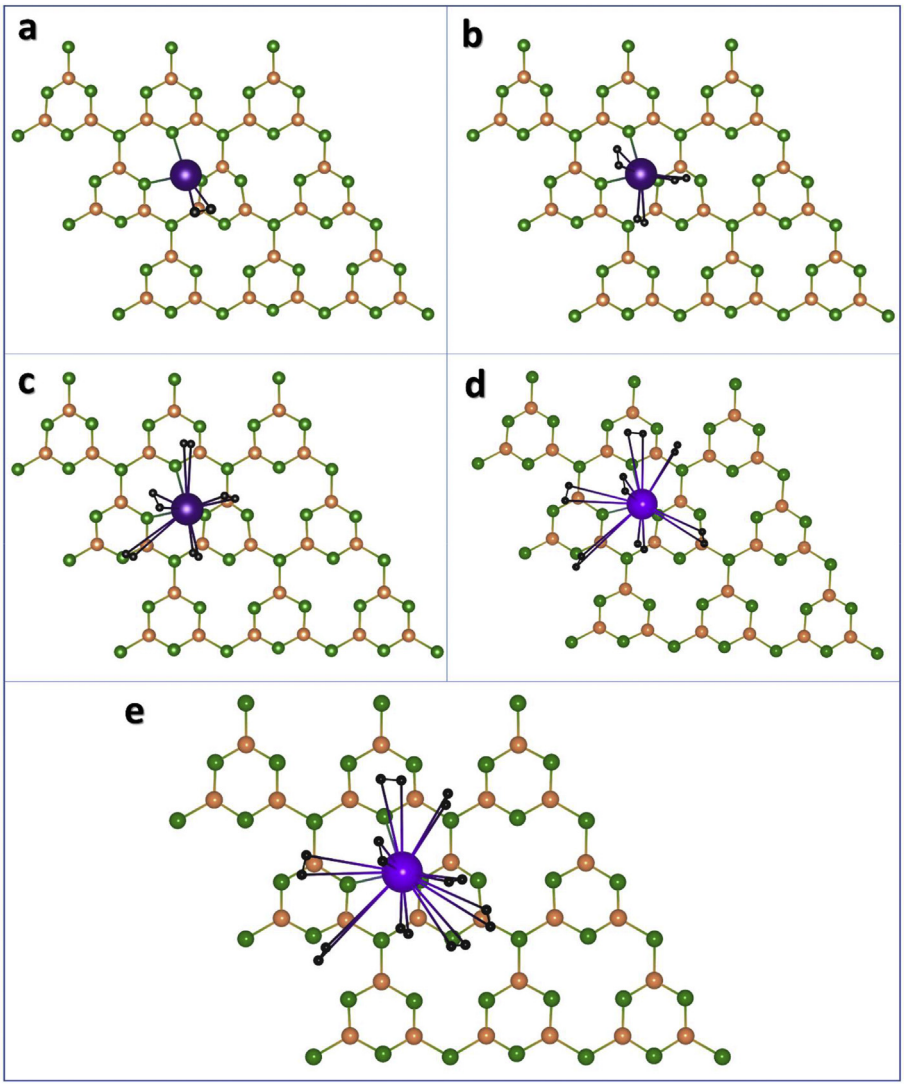

Fig. 4 – Relaxed structural plots of gCN + Y+1H_2 (a), gCN + Y+3H_2(b), gCN + Y+5H_2 (c), gCN + Y+7H_2 (d) and gCN + Y+9H_2 (e) with hydrogen atoms represented by black spheres.

our maximum H_2 adsorption estimates. We have not considered the 18 electron rule for maximum H_2 uptake because it may not be valid for interactions between metal and ligands as suggested by Fair et al. [66]. The average adsorption energy calculated for the 9 adsorbed H_2 was found to be −0.331 eV which lies within the range suggested by the DOE. The average adsorption energy curve using both GGA and GGA + vDW for the H_2 molecules ranging from 1H_2–9H_2 is presented in Fig. 5.

Computation of desorption temperature & hydrogen weight percentage

The temperature of desorption of hydrogen from gCN + Y can be computed using the van't Hoff equation [48–50]:

$$T_d = \left(\frac{E_b}{k_B}\right)\left(\frac{\Delta S}{R} - \ln P\right)^{-1} \quad (3)$$

where T_d, E_b, k_B, ΔS, R, and P are the desorption temperature, binding energy, Boltzmann constant, entropy change of condensation of hydrogen, ideal gas constant, and pressure respectively. The mean calculated desorption temperature for the system is found to be 384.24 K at ambient pressures, which is optimum for fuel cell applications. To compute the hydrogen storage capacity of gCN + Y, we employed an alternate loading pattern of Y over gCN, wherein only alternate hollow spaces in between three triazine rings were decorated with Y, placing sufficient distance between neighboring Y atoms to prevent cohesive interactions that can lead to dimerization or clustering. The gravimetric storage capacity of gCN + Y, with Y decoration above and below the plane surface, is calculated to be 8.55%, which is higher than the DOE's requirement of 6.5% or higher for onboard hydrogen storage in light FCVs. We have presented the gCN loaded with 9 H_2 molecules for 8 Y atoms situated symmetrically above and below the plane in Fig. 6 with gravimetric weight percent of 8.55. For further details, we have provided the comparison table with the previous reported values and our present work in Table 1.

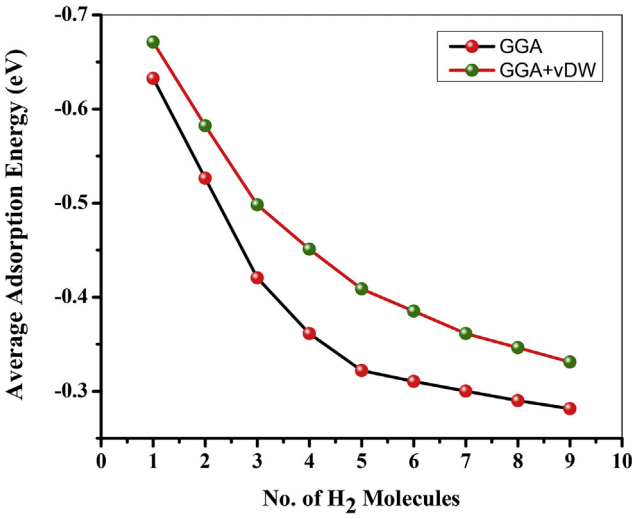

Fig. 5 – Average adsorption energy variation for GGA and GGA + vDW potentials corresponding to H_2 adsorption from $1H_2$–$9H_2$.

Insights on the interaction mechanism

The binding mechanism of Y over gCN and H_2 over gCN + Y has been investigated using the partial density of states (PDOS) where the orbital-wise density of states can be obtained for the interacting species, and charge transfer analysis.

Binding of Y over gCN

The binding of Y over gCN was observed to be accompanied by structural as well as electronic and magnetic changes. The mechanism of binding may involve a charge transfer, the intensity and direction of which are relevant to understanding the nature of binding. The partial density of states (PDOS) plots for valence 4d orbitals of Y in an isolated Y atom is compared with that in gCN + Y in the top and bottom panels respectively in Fig. 7(a), while C and N valence 2p orbitals in gCN are compared with that in gCN + Y in the top and bottom panels of Fig. 7(b) and (c) respectively. From the PDOS plots, it is noted that states of Y 4d orbital are depleted upon binding of Y on gCN at the Fermi level (~0 eV) (Fig. 7(a)). In the case of C and N 2p orbitals, some enhancements of states are noted near the Fermi level upon Y binding over gCN. For C 2p orbitals of gCN, an enhancement of states is noted in the valence band near the Fermi level (~-0.12 eV) upon binding of Y as compared to pristine gCN (Fig. 7(b)). Similar enhancement is noted in the case of N 2p orbitals in the valence band near the Fermi level (~-0.11 eV) (Fig. 7(c)).

This analysis may indicate some charge flow from the Y atom towards the C and N atoms of the gCN substrate. To get a quantitative picture of the charge transferred, we used Bader Charge Analysis [67]. It is observed that upon Y decoration over gCN, a charge of 1.653e is transferred from the Y atom towards gCN.The charge density distribution plot for the charge difference between gCN + Y and gCN is represented in Fig. 10(a). The intense red region around Y is indicative of charge loss, whereas green, blue, and yellow regions around

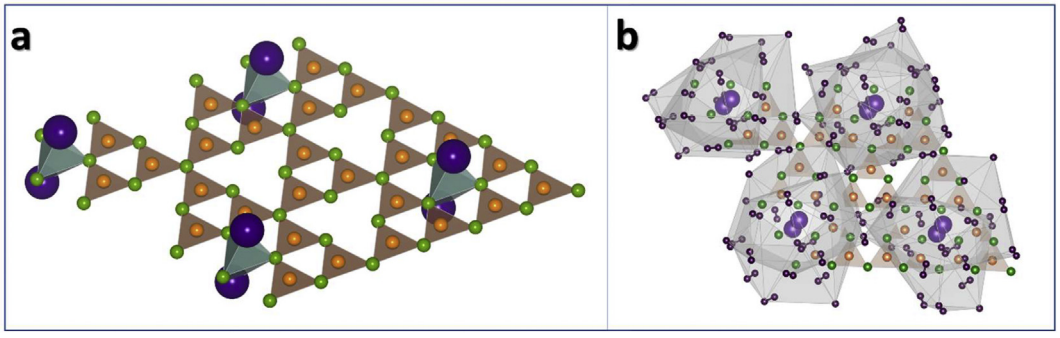

Fig. 6 – (a)Loading pattern of 8 Y atoms placed symmetrically on both sides of a 3 × 3 supercell of gCN with (b) hydrogen loading in the system represented. Gravimetric hydrogen storage capacity of the system considering such a loading pattern is 8.55%.

Table 1 – Hydrogen storage performance of various earlier reported materials.

System	Binding energy	Desorption temperature	Storage capacity	Reference
Ti-decorated B-doped twin graphene	> – 0.2 eV	–	4.95%	[69]
Li-decorated Graphene nanoribbon	– 0.263 eV	–	3.8%	[70]
Zr-decorated CTF-1	– 0.38 eV	442 K	7.1%	[45]
Ti-doped ψ-graphene	– 0.3 eV	387 K	13.14%	[41]
Y-doped C_{24}	– 0.37 eV	477 K	8.84%	[19]
Fe-embedded gCN	– 0.146 to –1.305 eV	–	–	[71]
Ru-embedded gCN	–0.152 to –2.208 eV	–	–	[71]
Os-embedded gCN	–0.663 to –2.452 eV	–	–	[71]
Y-decorated gCN	–0.365 eV	423.68 K	8.55%	This work

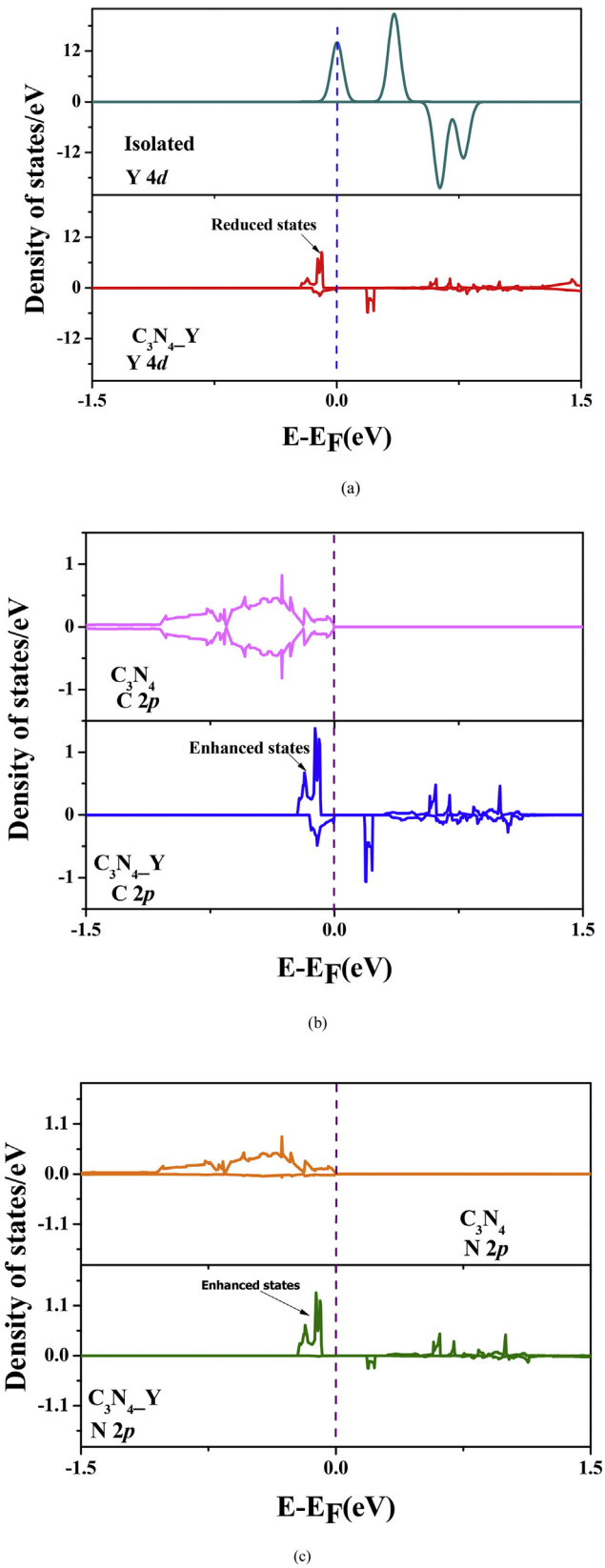

Fig. 7 – PDOS plots for comparison between gCN and gCN + Y 4d orbital of an isolated Y atom (top panel) is compared with that in gCN + Y (a), 2p orbital of C (b), and N in gCN is compared with that in gCN + Y in the top and bottom panels (c) respectively. Fermi level is set to zero.

gCN indicate a gain of charge. Thus, the Bader Charge Analysis, charge density distribution plot, and PDOS analysis point towards a charge-transfer-type interaction between Y atom and gCN wherein charges are transferred from 4d orbitals of Y atom towards the valence 2p orbitals of C and N in gCN.

Adsorption of H_2 over gCN + Y

The PDOS plot of Y 4d orbitals in gCN + Y is compared with that of gCN + Y+ $1H_2$ systems in Fig. 8(a), wherein a loss of states is noted around Fermi level in the regions of the valence band (~-0.08 to −0.13 eV) upon adsorption of H_2 on the gCN + Y system. On the other hand, the PDOS of 1s orbital of hydrogen in an isolated H_2 molecule is compared with that in the gCN + Y+ $1H_2$ system in Fig. 8(b). From the plot, it is observed that the 1s orbital of H_2 appears to gain states near the Fermi

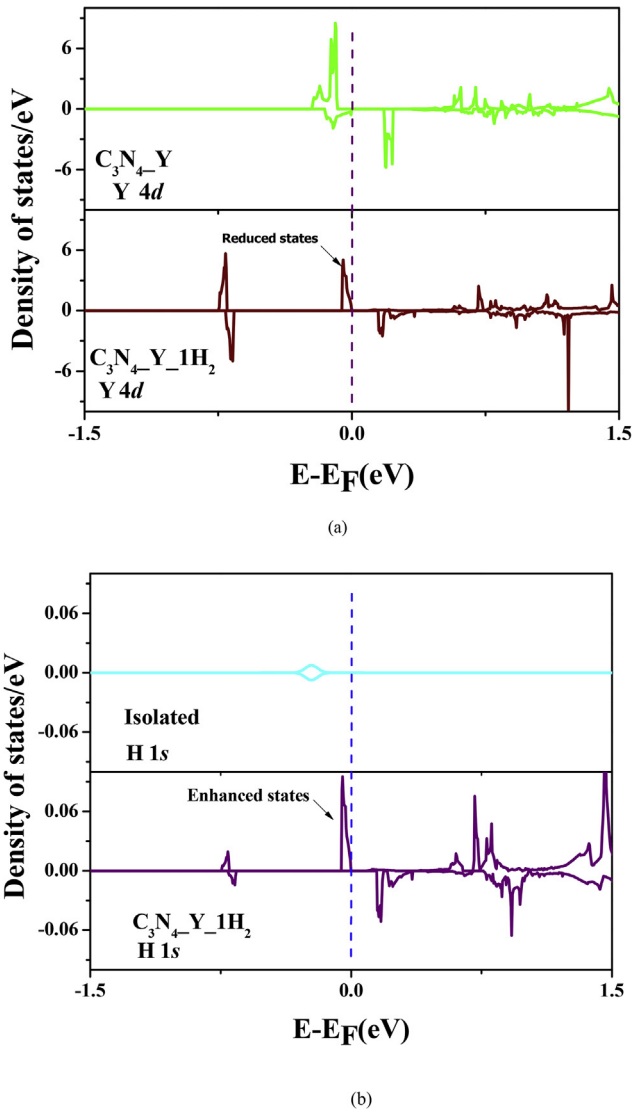

Fig. 8 – PDOS plot comparing 4d orbitals of Y atom in gCN + Y (top panel) against that in gCN + H_2 (lower panel) (a), and 1s orbitals of H in isolated H_2 molecule compared with that in gCN + Y+$1H_2$ (b). Fermi level is set to zero eV.

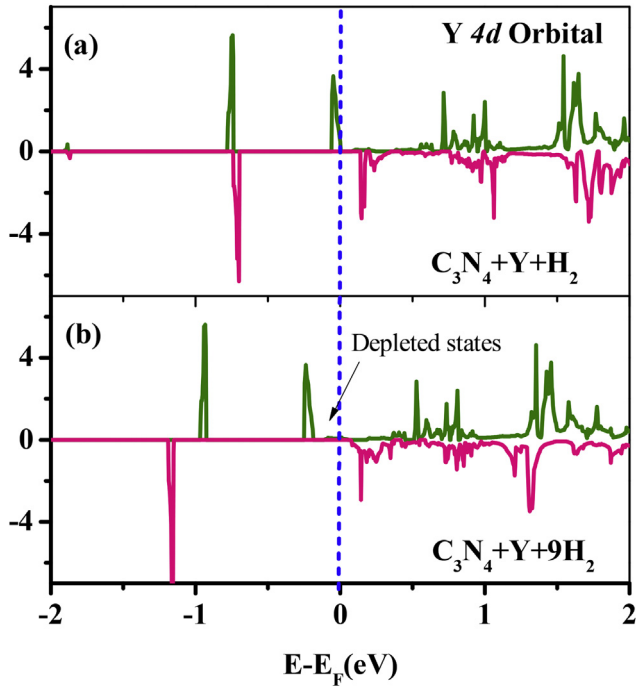

Fig. 9 – PDOS for Y 4d orbital for gCN + H_2 (a), and gCN+9H_2 (b); Fermi level is set tozero.

level in the valence band (sharp increase near ~ 0 eV) and a small spike appears between ~ −0.67 to −0.75 eV, indicating a possible charge transfer from Y atom towards H_2 upon binding. Since H–H bond lengths greater than 1.6 Å [53] are considered to be dissociative, in this case, the hydrogen binding may not be via a dissociative mechanism. The H–H bond lengths upon binding were 0.78 Å, i.e., only slightly elongated as compared to that of free H_2 molecules. This mechanism is similar to Kubas type of interactions providing adsorption energy higher than physisorption energy yet retaining the hydrogen in molecular form. With the loading of a higher number of H_2 molecules, Y 4d orbital continues to transfer charge to H 1s-orbital required for Kubas type of bonding. The PDOS for Y 4d orbital for gCN + Y + H_2 and gCN + Y+9H_2 systems are presented in Fig. 9(a and b). There is a reduction of states near the Fermi level for the system with a higher number of adsorbed H_2 molecules.

To verify this quantitatively, Bader Charge Analysis was conducted to compute the charge difference between gCN + Y and gCN + Y + H_2. The Y atom is found to lose 0.044e to H_2, with H_2 gaining 0.026e on an average upon adsorption over gCN + Y.

A qualitative idea about charge transfer is obtained from the charge density distribution plot for charge density difference between gCN + Y and gCN + Y + nH_2 where n = 1, 3, 5, 9 (Fig. 10(b-e)). The blue region denotes the charge gaining H_2 molecule whereas the charge losing gCN + Y is depicted in yellow-green color. As more H_2 pairs are adsorbed, the regions around gCN + Y become more green, indicating a smaller extent of charge transfer. This aligns well with the decreasing trend in adsorption energy as well as the increasing trend of Y–H bond lengths as more H_2 molecules are bound. Notably, the charge transferred to the H_2 molecules is not only contributed by the metal dopant, but also includes the charge transferred by the surface atoms, which is lesser for the nearest three H_2 molecules. Thus, the adsorption of 9 H_2 is not merely over the Y atom but is the result of H_2 adsorption over the whole system (surface + metal). This qualitative picture is in agreement with the earlier observed PDOS and Bader analysis.

Practical viability: Clustering and MD simulations

DFT simulations provide a rapid screening method for novel materials and their possible applications. However, to assess their practical viability, issues like the possibility of TM clustering and system stability at ambient temperatures as well as desorption temperatures will have to be considered. These aspects are discussed in the following sub-sections.

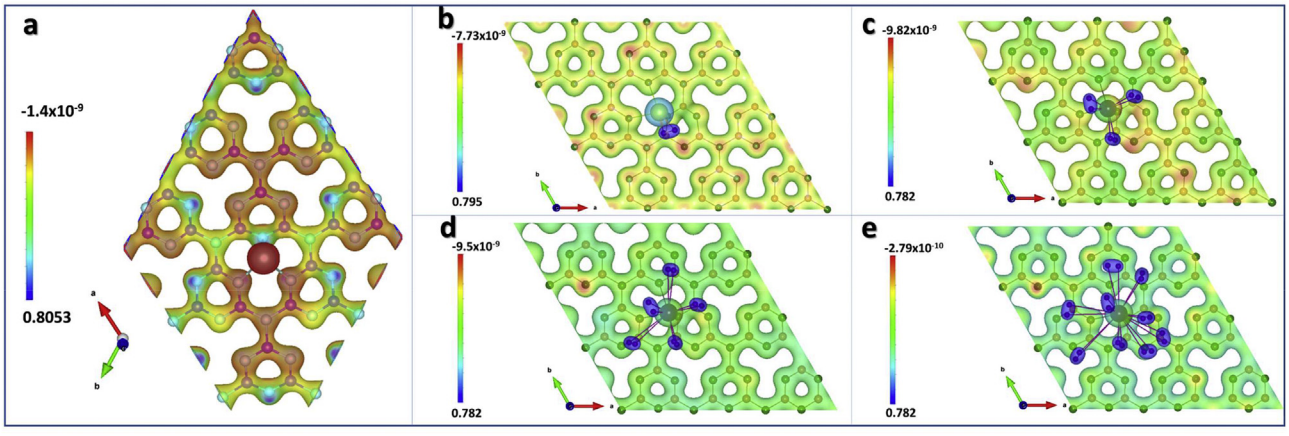

Fig. 10 – (a) Charge density distribution plot for Difference in charge density of gCN before and after Y decoration, i.e. [$\rho_{gCN+Y} - \rho_{gCN} - \rho_Y$] with isovalue = 0.079; and the difference in charge density of gCN + Y before and after adsorption of (b) 1, (c) 3, (d) 5, (e) 9H_2, i.e., [$\rho_{gCN+Y+H2} - \rho_{gCN+Y} - \rho_{H2}$] having isovalue of 0.09 e (b). Blue and green regions indicate charge gain, while red regions represent charge depletion. (For interpretation of the references to color in this figure legend, the reader is referred to the Web version of this article.)

Computation of diffusion energy barrier

Transition metals tend to cluster or dimerize due to their high cohesive energy. When decorated on a 2D surface like that of gCN, the computed gravimetric storage capacity will be impacted by metal-metal clustering. To address this possibility, we have computed the diffusion energy barrier for the Y atom across the 2D gCN structure. The computation of the diffusion energy barrier is carried out by non-relaxed single-step energy calculations across the path of diffusion of Y atom. Fig. 11 depicts the normalized energy value plot against displacement of Y atom from the least energy position, with the diffusion path shown inset. Since the value of the binding energy of Y on gCN is lower (−6.852 eV) than the cohesive energy of Y (−4.37 eV) [68], the chances of metal-metal clustering are negligible.

Structural stability from molecular dynamics simulations

Two important aspects to achieve reversible hydrogen storage are that at ambient temperatures, the Y atom must not dislodge from gCN, and any other structural distortions that can affect the reversibility of hydrogen storage do not occur. To this end, we have conducted ab initio MD simulations in a two-step process. In the first step, we raised the temperature of the system in 1 femtosecond time steps for 5 picoseconds in a microcanonical or NVE ensemble from 0 to 500 K. Thereafter, the structure at 500 K was allowed to attain equilibrium at 500 K by constant heating in a canonical or NVT ensemble for another 5 picoseconds. Temperature control was accomplished by the Nosé–Hoover thermostat. The MD snapshot of gCN + Y at 500 K for a single Y after attaining equilibrium is represented in Fig. 12(a) and two locations decorated with 2 Y are depicted in Fig. 12(b and c). The doping locations are alternated to ensure a sufficient distance between Y atoms so as to prevent metal-metal clustering interactions. It is found that the Y atom remains firmly bound to the gCN sheet at elevated temperature, and further, the gCN structure suffers very little distortions at this temperature. From the MD simulations, we are confident that the structural integrity of gCN + Y is not compromised at ambient temperatures.

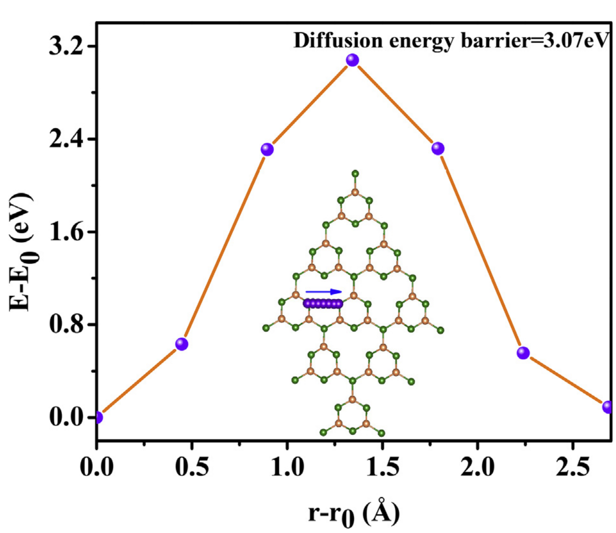

Fig. 11 – Diffusion energy barrier for the movement of Y atom in the path shown by arrow inside the structure embedded in the plot.

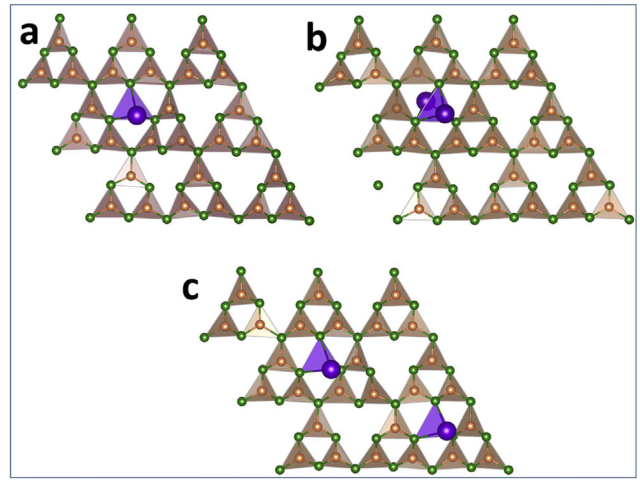

Fig. 12 – MD Snapshots of gCN + Y (a), gCN + 2Y in the same plane (b), and gCN + 2Y on the above and below the plane (c) at 500 K after 5 ps.

Conclusions

Using First Principles calculations, we have investigated the possibility of using Y-decorated gCN for onboard hydrogen storage applications in light vehicles in keeping with the requirements of the DOE. The probable site for Y decoration has been reported from adsorption energy calculations. Each Y atom decorated over gCN is found to reversibly adsorb a maximum of 9 molecules of hydrogen, giving a net binding capacity of 8.55 wt%; and the average adsorption energy per hydrogen molecule for gCN + Y+9H_2 is −0.331 eV and the corresponding desorption temperature is 384.24K, fulfilling DOE's criteria. The stability of gCN + Y was confirmed at ambient temperatures of 500 K via ab-initio MD simulations. The possibility of clustering of Y atoms is found to be negligible as the computed barrier energy for the diffusion of Y atoms across gCN is 3.07 eV. We have explored the stratagem of binding of Y over gCN and hydrogen over gCN + Y utilizing the orbital interactions via PDOS analysis and charge transfer calculations. The Y atom is found to bind strongly with gCN with a flow of charge from Y atom 4d orbital towards valence 2p orbitals of C and N in gCN, whereas the binding of hydrogen may follow Kubas type of binding involving H_2 to Y charge transfer followed by back donation. From our systematic study, we are confident in the potential of gCN + Y for reversible hydrogen storage applications for onboard storage needs in light vehicles.

Declaration of competing interest

The authors declare that they have no known competing financial interests or personal relationships that could have appeared to influence the work reported in this paper.

Acknowledgments

Dr. B. Chakraborty would like to thank Dr. Nandini Garg, Dr. T. Sakuntala, Dr. S.M. Yusuf, and Dr. A. K Mohanty for their great support and encouragement, and the staff of BARC computer division for availing supercomputing facility. BC would also like to thank Beetihotra Chakraborty for the help. PM appreciates the support of Dr. Ajit Kundu in this work. AV would like to thank Dr. Vaibhav Salvi and Dr. Vaibhav Wagh for their immense help.

Appendix A. Supplementary data

Supplementary data to this article can be found online at https://doi.org/10.1016/j.ijhydene.2022.04.184.

REFERENCES

[1] Thomas JM, Edwards PP, Dobson PJ, Owen GP. Decarbonising energy: the developing international activity in hydrogen technologies and fuel cells. J Energy Chem 2020;51:405–15. https://doi.org/10.1016/j.jechem.2020.03.087.

[2] Ajanovic A, Haas R. Prospects and impediments for hydrogen and fuel cell vehicles in the transport sector. Int J Hydrogen Energy 2021;46:10049–58. https://doi.org/10.1016/j.ijhydene.2020.03.122.

[3] Ajanovic A, Glatt A, Haas R. Prospects and impediments for hydrogen fuel cell buses. Energy 2021;235:121340. https://doi.org/10.1016/j.energy.2021.121340.

[4] Ishaq T, Yousaf M, Bhatti IA, Batool A, Asghar MA, Mohsin M, Ahmad M. A perspective on possible amendments in semiconductors for enhanced photocatalytic hydrogen generation by water splitting. Int J Hydrogen Energy 2021;46:39036–57. https://doi.org/10.1016/j.ijhydene.2021.09.165.

[5] Patel K, Baraiya BA, Som NN, Roondhe B, Jha PK. Investigating hydrogen evolution reaction properties of a new honeycomb 2D AlC. Int J Hydrogen Energy 2020;45:18602–11. https://doi.org/10.1016/j.ijhydene.2019.10.131.

[6] Zhang Q, Jiao S, Wang B, Wang Z, Lv X, Wang W, Tan Y, Cui C, Chen Y. Accelerate the alkaline hydrogen evolution reaction of the heterostructural Ni2P@Ni(OH)2/NF by dispersing a trifle of Ru on the surface. Int J Hydrogen Energy 2021;46:26329–39. https://doi.org/10.1016/j.ijhydene.2021.05.136.

[7] Sharma V, Kagdada HL, Wang J, Jha PK. Hydrogen adsorption on pristine and platinum decorated graphene quantum dot: a first principle study. Int J Hydrogen Energy 2020;45:23977–87. https://doi.org/10.1016/j.ijhydene.2019.09.021.

[8] Dafedar AA, Verma SS, Yadav A. Hydrogen storage techniques for stationary and mobile applications: a review. In: Jha K, Gulati P, Tripathi UK, editors. Recent advances in sustainable technologies. Singapore: Springer; 2021. p. 29–40. https://doi.org/10.1007/978-981-16-0976-3_4.

[9] Davoodabadi A, Mahmoudi A, Ghasemi H. The potential of hydrogen hydrate as a future hydrogen storage medium. iScience 2021;24:101907. https://doi.org/10.1016/j.isci.2020.101907.

[10] Moradi R, Groth KM. Hydrogen storage and delivery: review of the state of the art technologies and risk and reliability analysis. Int J Hydrogen Energy 2019;44:12254–69. https://doi.org/10.1016/j.ijhydene.2019.03.041.

[11] Preuster P, Papp C, Wasserscheid P. Liquid organic hydrogen Carriers (LOHCs): toward a hydrogen-free hydrogen economy. Acc Chem Res 2017;50:74–85. https://doi.org/10.1021/acs.accounts.6b00474.

[12] Teichmann D, Arlt W, Wasserscheid P. Liquid Organic Hydrogen Carriers as an efficient vector for the transport and storage of renewable energy. Int J Hydrogen Energy 2012;37:18118–32. https://doi.org/10.1016/j.ijhydene.2012.08.066.

[13] Tarhan C, Çil MA. A study on hydrogen, the clean energy of the future: hydrogen storage methods. J Energy Storage 2021;40:102676. https://doi.org/10.1016/j.est.2021.102676.

[14] DOE Technical Targets for Onboard Hydrogen Storage for Light-Duty Vehicles, Energy. (n.d.). https://www.energy.gov/eere/fuelcells/doe-technical-targets-onboard-hydrogen-storage-light-duty-vehicles (accessed May 13, 2021).

[15] Zaluska A, Zaluski L, Ström-Olsen JO. Structure, catalysis and atomic reactions on the nano-scale: a systematic approach to metal hydrides for hydrogen storage. Appl Phys A 2001;72:157–65. https://doi.org/10.1007/s003390100783.

[16] Imamura H, Masanari K, Kusuhara M, Katsumoto H, Sumi T, Sakata Y. High hydrogen storage capacity of nanosized magnesium synthesized by high energy ball-milling. J Alloys Compd 2005;386:211–6. https://doi.org/10.1016/j.jallcom.2004.04.145.

[17] Zaluski L, Zaluska A, Ström-Olsen JO. Nanocrystalline metal hydrides. J Alloys Compd 1997;253–254:70–9. https://doi.org/10.1016/S0925-8388(96)02985-4.

[18] Zaluska A, Zaluski L, Ström–Olsen JO. Nanocrystalline magnesium for hydrogen storage. J Alloys Compd 1999;288:217–25. https://doi.org/10.1016/S0925-8388(99)00073-0.

[19] Rusman NAA, Dahari M. A review on the current progress of metal hydrides material for solid-state hydrogen storage applications. Int J Hydrogen Energy 2016;41:12108–26. https://doi.org/10.1016/j.ijhydene.2016.05.244.

[20] Okada M, Kuriiwa T, Kamegawa A, Takamura H. Role of intermetallics in hydrogen storage materials. Mater Sci Eng 2002;329–331:305–12. https://doi.org/10.1016/S0921-5093(01)01580-5.

[21] Szajek A, Jurczyk M, Okońska I, Smardz K, Jankowska E, Smardz L. Electrochemical and electronic properties of nanocrystalline Mg-based hydrogen storage materials. J Alloys Compd 2007;436:345–50. https://doi.org/10.1016/j.jallcom.2006.07.043.

[22] Liu S, Liu J, Liu X, Shang J, Xu L, Yu R, Shui J. Hydrogen storage in incompletely etched multilayer Ti2CTx at room temperature. Nat Nanotechnol 2021;16:331–6. https://doi.org/10.1038/s41565-020-00818-8.

[23] Zhao W, Fierro V, Zlotea C, Izquierdo MT, Chevalier-César C, Latroche M, Celzard A. Activated carbons doped with Pd nanoparticles for hydrogen storage. Int J Hydrogen Energy 2012;37:5072–80. https://doi.org/10.1016/j.ijhydene.2011.12.058.

[24] Lee S-Y, Park S-J. Effect of platinum doping of activated carbon on hydrogen storage behaviors of metal-organic frameworks-5. Int J Hydrogen Energy 2011;36:8381–7. https://doi.org/10.1016/j.ijhydene.2011.03.038.

[25] Wang Y, Wang K, Guan C, He Z, Lu Z, Chen T, Liu J, Tan X, Yang Tan TT, Li CM. Surface functionalization-enhanced spillover effect on hydrogen storage of Ni–B nanoalloy-doped activated carbon. Int J Hydrogen Energy 2011;36:13663–8. https://doi.org/10.1016/j.ijhydene.2011.08.049.

[26] Wang L, Quadir MZ, Aguey-Zinsou K-F. Partially reversible hydrogen storage of lithium hydride (LiH) nanoconfined in high surface area graphite. Int J Hydrogen Energy

2016;41:18088–94. https://doi.org/10.1016/j.ijhydene.2016.07.073.
[27] Gangu KK, Maddila S, Mukkamala SB, Jonnalagadda SB. Characteristics of MOF, MWCNT and graphene containing materials for hydrogen storage: a review. J Energy Chem 2019;30:132–44. https://doi.org/10.1016/j.jechem.2018.04.012.
[28] Öztürk Z. Lithium decoration characteristics for hydrogen storage enhancement in novel periodic porous graphene frameworks. Int J Hydrogen Energy 2021;46:11804–14. https://doi.org/10.1016/j.ijhydene.2021.01.073.
[29] Mahamiya V, Shukla A, Chakraborty B. Exploring yttrium doped C24 fullerene as a high-capacity reversible hydrogen storage material: DFT investigations. J Alloys Compd 2022;897:162797. https://doi.org/10.1016/j.jallcom.2021.162797.
[30] Xu W-C, Takahashi K, Matsuo Y, Hattori Y, Kumagai M, Ishiyama S, Kaneko K, Iijima S. Investigation of hydrogen storage capacity of various carbon materials. Int J Hydrogen Energy 2007;32:2504–12. https://doi.org/10.1016/j.ijhydene.2006.11.012.
[31] Zhao W, Fierro V, Fernández-Huerta N, Izquierdo MT, Celzard A. Impact of synthesis conditions of KOH activated carbons on their hydrogen storage capacities. Int J Hydrogen Energy 2012;37:14278–84. https://doi.org/10.1016/j.ijhydene.2012.06.110.
[32] Mohan M, Sharma VK, Kumar EA, Gayathri V. Hydrogen storage in carbon materials—a review. Energy Storage 2019;1:e35. https://doi.org/10.1002/est2.35.
[33] Lavanya R, Surya VJ, Lakshmi I, Iyakutti K, Vasu V, Mizuseki H, Kawazoe Y. Hydrogen storage in TiO2 functionalized (10, 10) single walled carbon nanotube (SWCNT) – first principles study. Int J Hydrogen Energy 2014;39:4973–80. https://doi.org/10.1016/j.ijhydene.2014.01.048.
[34] Chakraborty B, Modak P, Banerjee S. Hydrogen storage in yttrium-decorated single walled carbon nanotube. J Phys Chem C 2012;116:22502–8. https://doi.org/10.1021/jp3036296.
[35] ullah Rather S, Taimoor AA, Muhammad A, Alhamed YA, Zaman SF, Ali AM. Kinetics of hydrogen adsorption on MgH2/CNT composite. Mater Res Bull 2016;77:23–8. https://doi.org/10.1016/j.materresbull.2016.01.025.
[36] Subrahmanyam KS, Vivekchand SRC, Govindaraj A, Rao CNR. A study of graphenes prepared by different methods: characterization, properties and solubilization. J Mater Chem 2008;18:1517–23. https://doi.org/10.1039/B716536F.
[37] Hao J, Wei F, Zhang X, Li L, Chen C, Wu G, Wu L, Liang D, Ma X, Lu P, Song H. An investigation of Li-decorated N-doped penta-graphene for hydrogen storage. Int J Hydrogen Energy 2021;46:25533–42. https://doi.org/10.1016/j.ijhydene.2021.05.089.
[38] Kostoglou N, Tarat A, Walters I, Ryzhkov V, Tampaxis C, Charalambopoulou G, Steriotis T, Mitterer C, Rebholz C. Few-layer graphene-like flakes derived by plasma treatment: a potential material for hydrogen adsorption and storage. Microporous Mesoporous Mater 2016;225:482–7. https://doi.org/10.1016/j.micromeso.2016.01.027.
[39] Vinayan BP, Nagar R, Ramaprabhu S. Solar light assisted green synthesis of palladium nanoparticle decorated nitrogen doped graphene for hydrogen storage application. J Mater Chem A 2013;1:11192–9. https://doi.org/10.1039/C3TA12016C.
[40] Yuan L, Kang L, Chen Y, Wang D, Gong J, Wang C, Zhang M, Wu X. Hydrogen storage capacity on Ti-decorated porous graphene: first-principles investigation. Appl Surf Sci 2018;434:843–9. https://doi.org/10.1016/j.apsusc.2017.10.231.
[41] Chakraborty B, Ray P, Garg N, Banerjee S. High capacity reversible hydrogen storage in titanium doped 2D carbon allotrope Ψ-graphene: density Functional Theory investigations. Int J Hydrogen Energy 2021;46:4154–67. https://doi.org/10.1016/j.ijhydene.2020.10.161.
[42] Isidro-Ortega FJ, Pacheco-Sánchez JH, Desales-Guzmán LA. Hydrogen storage on lithium decorated zeolite templated carbon, DFT study. Int J Hydrogen Energy 2017;42:30704–17. https://doi.org/10.1016/j.ijhydene.2017.10.098.
[43] Isidro-Ortega FJ, Pacheco-Sánchez JH, González-Ruíz A, Alejo R. DFT study of hydrogen storage on the metallic decoration of boron substitution on zeolite templated carbon vacancy. Int J Hydrogen Energy 2020;45:19505–15. https://doi.org/10.1016/j.ijhydene.2020.05.017.
[44] Tuci G, Iemhoff A, Rossin A, Yakhvarov D, Gatto MF, Balderas-Xicohténcatl R, Zhang L, Hirscher M, Palkovits R, Pham-Huu C, Giambastiani G. Tailoring morphological and chemical properties of covalent triazine frameworks for dual CO2 and H2 adsorption. Int J Hydrogen Energy 2022;47:8434–45. https://doi.org/10.1016/j.ijhydene.2021.12.197.
[45] Vaidyanathan A, Wagh V, Rout CS, Chakraborty B. High capacity reversible hydrogen storage in zirconium doped 2D-covalent triazine frameworks: density Functional Theory investigations. Int J Hydrogen Energy 2021;46:14520–31. https://doi.org/10.1016/j.ijhydene.2021.01.175.
[46] Gao P, Liu Z, Zhang F. Computational evaluation of Li-doped g-C2N monolayer as advanced hydrogen storage media. Int J Hydrogen Energy 2022;47:3625–32. https://doi.org/10.1016/j.ijhydene.2021.11.003.
[47] Chen X, Li J, Dou X, Gao P. Computational evaluation of Mg-decorated g-CN as clean energy gas storage media. Int J Hydrogen Energy 2021;46:35130–6. https://doi.org/10.1016/j.ijhydene.2021.08.071.
[48] Hao L, Ning J, Luo B, Wang B, Zhang Y, Tang Z, Yang J, Thomas A, Zhi L. Structural evolution of 2D microporous covalent triazine-based framework toward the study of high-performance supercapacitors. J Am Chem Soc 2015;137:219–25. https://doi.org/10.1021/ja508693y.
[49] Zhao Z, Sun Y, Dong F. Graphitic carbon nitride based nanocomposites: a review. Nanoscale 2015;7:15–37. https://doi.org/10.1039/C4NR03008G.
[50] Algara-Siller G, Severin N, Chong SY, Björkman T, Palgrave RG, Laybourn A, Antonietti M, Khimyak YZ, Krasheninnikov AV, Rabe JP, Kaiser U, Cooper AI, Thomas A, Bojdys MJ. Triazine-based graphitic carbon nitride: a two-dimensional semiconductor. Angew Chem Int Ed 2014;53:7450–5. https://doi.org/10.1002/anie.201402191.
[51] Tan X, Kou L, Tahini HA, Smith SC. Charge modulation in graphitic carbon nitride as a switchable approach to high-capacity hydrogen storage. ChemSusChem 2015;8:3626–31. https://doi.org/10.1002/cssc.201501082.
[52] Nair AAS, Sundara R, Anitha N. Hydrogen storage performance of palladium nanoparticles decorated graphitic carbon nitride. Int J Hydrogen Energy 2015;40:3259–67. https://doi.org/10.1016/j.ijhydene.2014.12.065.
[53] Kubas GJ. Fundamentals of H2 binding and reactivity on transition metals underlying hydrogenase function and H2 production and storage. Chem Rev 2007;107:4152–205. https://doi.org/10.1021/cr050197j.
[54] Ströbel R, Garche J, Moseley PT, Jörissen L, Wolf G. Hydrogen storage by carbon materials. J Power Sources 2006;159:781–801. https://doi.org/10.1016/j.jpowsour.2006.03.047.
[55] Kresse G, Furthmüller J. Efficiency of ab-initio total energy calculations for metals and semiconductors using a plane-wave basis set. Comput Mater Sci 1996;6:15–50. https://doi.org/10.1016/0927-0256(96)00008-0.
[56] Kresse G, Hafner J. Ab initio molecular dynamics for liquid metals. Phys Rev B 1993;47:558–61. https://doi.org/10.1103/PhysRevB.47.558.

[57] Kresse G, Hafner J. Ab initio molecular-dynamics simulation of the liquid-metal–amorphous-semiconductor transition in germanium. Phys Rev B 1994;49:14251–69. https://doi.org/10.1103/PhysRevB.49.14251.
[58] Lugo-Solis A, Vasiliev I. Ab initio study of K adsorption on graphene and carbon nanotubes: role of long-range ionic forces. Phys Rev B 2007;76:235431. https://doi.org/10.1103/PhysRevB.76.235431.
[59] Perdew JP, Burke K, Ernzerhof M. Generalized gradient approximation made simple. Phys Rev Lett 1996;77:3865–8. https://doi.org/10.1103/PhysRevLett.77.3865.
[60] Kelkkanen AK, Lundqvist BI, Nørskov JK. Density functional for van der Waals forces accounts for hydrogen bond in benchmark set of water hexamers. J Chem Phys 2009;131:046102. https://doi.org/10.1063/1.3193462.
[61] Grimme S. Semiempirical GGA-type density functional constructed with a long-range dispersion correction. J Comput Chem 2006;27:1787–99. https://doi.org/10.1002/jcc.20495.
[62] Heyd J, Scuseria GE. Efficient hybrid density functional calculations in solids: assessment of the Heyd–Scuseria–Ernzerhof screened Coulomb hybrid functional. J Chem Phys 2004;121:1187–92. https://doi.org/10.1063/1.1760074.
[63] Molina B, Sansores LE. Electronic structure of six phases of c3n4: a theoretical approach. Mod Phys Lett B 1999;13:193–201. https://doi.org/10.1142/S0217984999000269.
[64] Heyd J, Scuseria GE, Ernzerhof M. Hybrid functionals based on a screened Coulomb potential. J Chem Phys 2003;118:8207–15. https://doi.org/10.1063/1.1564060.
[65] Wang X, Blechert S, Antonietti M. Polymeric graphitic carbon nitride for heterogeneous photocatalysis. ACS Catal 2012;2:1596–606. https://doi.org/10.1021/cs300240x.
[66] Fair KM, Cui XY, Li L, Shieh CC, Zheng RK, Liu ZW, Delley B, Ford MJ, Ringer SP, Stampfl C. Hydrogen adsorption capacity of adatoms on double carbon vacancies of graphene: a trend study from first principles. Phys Rev B 2013;87:014102. https://doi.org/10.1103/PhysRevB.87.014102.
[67] Arnaldsen, A.; Tang, W.; Henkelman, G, Bader charge analysis, (n.d.). http://theory.cm.utexas.edu/henkelman/code/bader/(accessed June 17, 2021).
[68] Kittel C. Introduction to solid state physics. 8th ed. Wiley, John Wiley & Sons, Inc.; 2004. https://www.wiley.com/en-us/Introduction+to+Solid+State+Physics%2C+8th+Edition-p-9780471415268. [Accessed 2 February 2022].
[69] Dong S, Lv E, Wang J, Li C, Ma K, Gao Z, Yang W, Ding Z, Wu C, Gates ID. Construction of transition metal-decorated boron doped twin-graphene for hydrogen storage: a theoretical prediction. Fuel 2021;304:121351. https://doi.org/10.1016/j.fuel.2021.121351.
[70] Zheng N, Yang S, Xu H, Lan Z, Wang Z, Gu H. A DFT study of the enhanced hydrogen storage performance of the Li-decorated graphene nanoribbons. Vacuum 2020;171:109011. https://doi.org/10.1016/j.vacuum.2019.109011.
[71] Habibi-Yangjeh A, Basharnavaz H. Remarkable improvement in hydrogen storage capabilities of graphitic carbon nitride nanosheets under selected transition metal embedding: a DFT study. Int J Hydrogen Energy 2021;46:33864–76. https://doi.org/10.1016/j.ijhydene.2021.07.197.